

Sensitivity of binary liquid thermal convection to confinement

Published in *Physics of Fluids* (2003), Vol. 15, pp. 2791-2802

E. Millour, G. Labrosse

Université Paris-Sud,

Laboratoire d'Informatique pour la Mécanique et les Sciences de l'Ingénieur
LIMSI-CNRS BP 133, 91403 ORSAY CEDEX, FRANCE.

E. Tric

Université Nice Sophia Antipolis,

Laboratoire Géosciences AZUR,

250 rue Albert Einstein, 06560 VALBONNE, FRANCE.

Abstract

The stable axisymmetric convective states of a binary liquid enclosed in a vertical cylinder heated from below are exhaustively and accurately identified by pseudo-spectral numerical integration. In order to gain some insight on the influence that nearby boundaries can exert on flow dynamics, three aspect ratios (1/2, 1 and 2), as well as two types of lateral kinematic boundary conditions (either no-slip or free-slip) are investigated. The ranges over which stable quiescent, oscillatory and steady convective states extend and coexist are given. The bifurcations leading to transitions from one branch of solutions to another, as well as those that occur along the oscillatory branch, are analyzed. The most significant effect of varying boundary conditions and aspect ratio involves the route from oscillatory to steady convection. For a given configuration, that route consists of a period doubling cascade followed by chaos, or a subcritical generalized Hopf (or Neimark-Sacker) bifurcation, or a homoclinic bifurcation. The dynamics of thermal convection of enclosed binary mixtures is clearly very sensitive to both boundary conditions and aspect ratio.

1 Introduction

Since the initial investigations of Bénard and Rayleigh, convection in horizontal fluid layers heated from below is a problem that has been extensively studied in the context of pattern formation, instabilities and dynamical behavior of nonlinear systems (see, for example, Cross and Hohenberg [1] and references therein). Convection in cylindrical enclosures of aspect ratios around unity is a topic that has drawn much attention over the past years. Experimental and numerical studies of the convective flows that arise beyond onset, as well as their secondary instabilities, are still ongoing, as exemplified by many recent publications (see, e.g., Müller, [2] Touihri *et al.*, [3] Hof *et al.*, [4] Leong, [5] among others). Such works typically focus on following the evolution of flows with Rayleigh number Ra (which accounts for the externally imposed thermal stress) in given cases (i.e. given aspect ratio Γ , fluid Prandtl number Pr and thermal boundary conditions). Despite these many contributions, the knowledge of all the solutions and bifurcations that arise in the Γ - Pr - Ra parameter space is so far incomplete.

Investigations on thermal convection of binary fluids began about 30 years ago (see Platten and Legros [6]). In these mixtures, solute mass fraction and temperature gradients are coupled by the Soret effect. According to the sign of the Soret coefficient, the solute (which we take to be the heaviest of the two components) migrates towards the warmer or colder part of the container, and an initially homogeneous mixture, once subjected to a thermal gradient, separates in composition. The resulting Soret-driven mass fraction gradient thus

induces a solutal buoyancy that works against or with the thermal one. Both sign and amplitude of the Soret coupling are accounted for in the dimensionless separation ratio ψ between solutal and thermal buoyancies. These compete when ψ is negative, and their interplay yields additional (compared to pure fluids in the same conditions) complex spatiotemporal behaviors, which can moreover arise as the quiescent state turns unstable. Over the past decades an impressive number of 2D studies has been published on this system (see for instance Kolodner *et al.*, [7] Barten *et al.*, [8] Lücke *et al.*, [9] and references therein), mainly focused on horizontally infinite or very extended layers. All point out the dynamical richness of this configuration and confirm the extreme sensitivity of thermal flows to the presence of solutal distributions, even when mass fraction amplitudes are very small.

Numerical explorations of these systems are harder to carry out than when pure fluid are considered. The dimension of the parameter space to investigate is higher (Γ , Pr , Ra , ψ and Lewis number Le). Moreover, the occurrence of time-dependent flows rising directly from the rest state implies extra numerical requirements. First, their exploration must be performed over significantly large durations in order to reach settled temporal behaviors. Secondly, the numerical scheme that is used must be consistent with the continuous space-time problem to solve.

Three-dimensional numerical simulation of the first bifurcations in binary liquid thermal convection cannot therefore be yet considered as feasible, and literature is so far devoid of any results of this kind. What has been done in 2D focuses on limited regions of parameter space and mainly on large aspect ratio enclosures. To this day, even the 3D linear stability of a quiescent layer in small aspect ratio cylindrical cells has not been fully explored. Such analyses have been performed, by Hardin *et al.* [10] and Mercader *et al.*, [11] but over limited ranges of parameters. The reason for this is that which mode (axisymmetrical or azimuthal) is the most destabilizing depends on all of the system's parameters (i.e. Γ , Pr , Le and ψ). Note that the (temporal and azimuthal) structure of the destabilizing mode is not necessarily that of the resulting non linear solution. Since it is known that in the pure fluid case, [4, 5] axisymmetrical and 3D states coexist over specific sub-domains (in Ra), such may also occur for binary liquids.

Experiments on convection of water-ethanol mixtures in long rectangular cells (of variable aspect ratio, length over height of the enclosure ranging from 15 to 21) by Kolodner [12] display a strong sensitivity of flow dynamics to the length of the apparatus. This feature was also obtained in the 2D numerical simulations of Batiste *et al.* [13, 14]. The present work tackles a specific aspect of the richness of 2D dynamics in thermal convection of a binary liquid. We analyze the non linear states that occur in axisymmetrical enclosures of small aspect ratios (radius over height ratio), namely $\Gamma = 1/2$, 1 and 2, and with two types of boundary conditions for the velocity on the circumference of the cylinder, either no-slip or free-slip. The former simply represents the presence of a rigid wall, whereas the latter is a crude approximation (capillary effects being discarded) of a straight free surface and the modeled system is then related to a liquid bridge (Wanschura *et al.* [15]).

From the forthcoming results, it will be inferred that thermal convection of a binary liquid is extremely sensitive to both aspect ratio and boundary conditions.

This paper is organized as follows: the equations ruling binary liquid thermal convection are given and discussed in Sec. 2. The numerical tool and methods used for the simulations are presented in Sec. 3. Results obtained for the six modeled configurations are given

and compared in Sec. 4, where the multitude of bifurcations that arise are detailed. Our conclusions are then summarized in Sec. 5.

2 Physical Model

2.1 Ruling equations

The usual Oberbeck-Boussinesq equations, Soret effect included, are considered. Using the height h of the layer, the thermal diffusion velocity over h , the imposed temperature difference ΔT (between bottom and top plates) and the Soret-induced mass fraction difference ΔC of the quiescent state as reference scales leads to the following set of dimensionless equations:

$$\frac{\partial \mathbf{v}}{\partial t} + (\mathbf{v} \cdot \nabla) \mathbf{v} = -\nabla p + Ra Pr (\theta + \psi \gamma) \mathbf{e}_z + Pr \nabla^2 \mathbf{v}, \quad (1)$$

$$\nabla \cdot \mathbf{v} = 0, \quad (2)$$

$$\frac{\partial \theta}{\partial t} + (\mathbf{v} \cdot \nabla) \theta = \mathbf{v} \cdot \mathbf{e}_z + \nabla^2 \theta, \quad (3)$$

$$\frac{\partial \gamma}{\partial t} + (\mathbf{v} \cdot \nabla) \gamma = \mathbf{v} \cdot \mathbf{e}_z + Le (\nabla^2 \gamma - \nabla^2 \theta), \quad (4)$$

where $\mathbf{v} = u\mathbf{e}_r + w\mathbf{e}_z$ is the velocity, \mathbf{e}_r and \mathbf{e}_z are respectively the radial and upward unit vectors. p , θ and γ denote departures from pressure, temperature and mass fraction static profiles. The four numbers that appear in the governing equations are

$$Ra = \frac{\alpha \Delta T g h^3}{\nu \kappa}, \quad \psi = \frac{\beta \Delta C}{\alpha \Delta T}, \quad Pr = \frac{\nu}{\kappa}, \quad Le = \frac{D}{\kappa},$$

where α and β are the (positive) thermal and solutal expansion coefficients, ν , κ and D are the momentum, heat and mass diffusivities, g is the gravitational acceleration. The last three numbers are constant for a given fluid and here set to $Pr = 1$, $Le = 0.1$ and $\psi = -0.2$ (values that roughly are those of a ^3He - ^4He mixture [17, 16]), leaving Ra as the main parameter of this study. Recall that taking ψ to be negative implies that solutal and thermal buoyancies compete.

All boundaries are impervious to matter. Temperatures are imposed on the horizontal walls, along with lateral thermal insulation. Top and bottom boundary conditions are:

$$\theta = \frac{\partial \theta}{\partial z} - \frac{\partial \gamma}{\partial z} = u = w = 0 \quad \text{for } z = \pm \frac{1}{2}.$$

Denoting the aspect ratio $\Gamma = R/h$, where R is the radius of the cylinder, the lateral conditions on the scalar fields are:

$$\frac{\partial \theta}{\partial r} = \frac{\partial \gamma}{\partial r} = 0 \quad \text{for } r = \Gamma.$$

As previously mentioned, two sets of kinematic lateral boundary conditions are considered:

$$(a) \text{ No-slip: } u = w = 0 \quad \text{for } r = \Gamma,$$

or

$$(b) \text{ Free-slip: } u = \frac{\partial w}{\partial r} = 0 \quad \text{for } r = \Gamma.$$

In all that follows, these will be referred to as (a) NS and (b) FS configurations.

N_z	30	40	50	60	80	100
$\delta\mathcal{E}$	4.210^{-7}	1.210^{-8}	5.410^{-11}	2.110^{-12}	5.110^{-13}	
$\delta\bar{\theta}$	2.810^{-5}	4.610^{-7}	5.710^{-9}	1.110^{-11}	4.410^{-11}	
$\bar{\gamma}$	1.110^{-7}	3.310^{-10}	1.510^{-10}	5.010^{-11}	9.110^{-12}	5.510^{-12}
d	4.310^{-4}	1.210^{-4}	2.510^{-5}	7.010^{-6}	9.010^{-6}	6.010^{-6}

Table 1: Evolution of global quantities with grid size. These values were obtained for a steady flow at $Ra = 3000$, in the $\Gamma = 2$ NS configuration, with a time step δt of $5 \cdot 10^{-4}$. Grids of $(2N_z + 1) \times (N_z + 1)$ nodes in $r \times z$ were used. $\delta\bar{\theta}$ and $\delta\mathcal{E}$ denote the relative difference to the overall temperature $\bar{\theta}_{ref} = -2.69562701076 \cdot 10^{-2}$ and kinetic energy $\mathcal{E}_{ref} = 1.5660498335843 \cdot 10^2$ obtained as references with $N_z = 100$. The last two lines of the table refer to the mean mass fraction $\bar{\gamma}$ in the enclosure ($\bar{\gamma}$ should be zero) and the relative velocity divergence d (see text).

2.2 Symmetries of the solutions

Since in the following sections the symmetries of both steady and time-dependent convective states will be of interest, we mention here that the up-down (or mirror symmetry, denoted \mathcal{M}) in the governing equations implies the following:

if $X_1 = (u_1, w_1, p_1, \theta_1, \gamma_1)$ satisfies equations (1-4), then so does $X_2 = (u_2, w_2, p_2, \theta_2, \gamma_2)$, provided that

$$\begin{aligned}
u_2(r, z, t) &= u_1(r, -z, t), \\
w_2(r, z, t) &= -w_1(r, -z, t), \\
p_2(r, z, t) &= p_1(r, -z, t), \\
\theta_2(r, z, t) &= -\theta_1(r, -z, t), \\
\gamma_2(r, z, t) &= -\gamma_1(r, -z, t).
\end{aligned}$$

Solutions therefore either come in pairs that transform into one another under \mathcal{M} or are invariant under such a transformation.

Periodic oscillations (of period τ) may possess a temporal symmetry \mathcal{T} relating solutions separated by half a period in the following way:

$$\begin{aligned}
u(r, z, t + \frac{\tau}{2}) &= u(r, -z, t), \\
w(r, z, t + \frac{\tau}{2}) &= -w(r, -z, t), \\
p(r, z, t + \frac{\tau}{2}) &= p(r, -z, t), \\
\theta(r, z, t + \frac{\tau}{2}) &= -\theta(r, -z, t), \\
\gamma(r, z, t + \frac{\tau}{2}) &= -\gamma(r, -z, t).
\end{aligned}$$

The role of temporal symmetry and its practical implications have been examined and clarified by Swift and Wiesenfeld. [18] The main result of their study is that in systems such as the one investigated here, time-symmetric oscillations cannot undergo period doubling bifurcations. These solutions are hence typically [19] found to first bifurcate to asymmetry before undergoing period doubling.

3 Numerical method

3.1 Spatial and temporal integrations

The set of governing equations is solved by a Chebyshev pseudo-spectral method in space and a second-order finite-differences scheme in time.

Gauss-Lobatto nodes are used in the vertical direction \mathbf{e}_z , located at

$$z_j = -\frac{1}{2} \cos\left(\frac{\pi j}{N_z}\right) \quad \text{with } j \in [0, N_z],$$

where N_z is the highest degree (cutoff frequency) of the Chebyshev polynomial expansion. Gauss-Radau nodes are used in the radial direction \mathbf{e}_r , located at

$$r_j = \frac{\Gamma}{2} \left(1 + \cos\left(\frac{2\pi(N_r - j)}{2N_r + 1}\right) \right) \quad \text{with } j \in [0, N_r].$$

Note that using a Gauss-Radau grid enables one to avoid the singularity at $r = 0$ and to implicitly impose the axisymmetry boundary conditions on the axis, namely $u = \frac{\partial w}{\partial r} = \frac{\partial \theta}{\partial r} = \frac{\partial \gamma}{\partial r} = 0$.

The cutoff frequencies N_r and N_z were chosen such that $N_r = \Gamma N_z$, which leads to grids of $(\Gamma N_z + 1)(N_z + 1)$ nodes.

Time integration is achieved by a second-order finite-differences approximation, using a three-level scheme for time derivatives, diffusion and advection terms respectively being evaluated implicitly and explicitly. Velocity and pressure fields are uncoupled via a specific projection-diffusion algorithm [20, 21] which is consistent, [22] in contrast to the well known time-splitting schemes, with the continuous uncoupled velocity-pressure problem. Pressure is first obtained by solving a quasi-Poisson operator without having to impose any boundary condition on this field. Velocity is then obtained by solving a standard unsteady diffusion equation with a divergence-free right hand side. Since the numerical divergence of any analytically known divergence-free field cannot exactly cancel but only asymptotically with node number, this approach yields, by truncation, an asymptotically solenoidal velocity. This has been commented at length by Tric *et al.*, [23] who obtained the expected exponential decrease of $\nabla \cdot \mathbf{v}$ with cutoff frequencies in computations of thermally driven pure fluid convection in a cubical cavity.

3.2 Accuracy assessments

3.2.1 Spatial convergence

Using a pseudo-spectral approach leads to expect an exponential improvement of numerical solutions with increasing cutoff frequencies. This has been checked using the following global instantaneous quantities:

$$\begin{aligned} \mathcal{E} &= 2\pi \int_{r=0}^{r=\Gamma} \int_{z=-1/2}^{z=1/2} \frac{\mathbf{v} \cdot \mathbf{v}}{2} r dr dz \quad , \\ \bar{\theta} &= 2\pi \int_{r=0}^{r=\Gamma} \int_{z=-1/2}^{z=1/2} \theta r dr dz \quad , \\ \bar{\gamma} &= 2\pi \int_{r=0}^{r=\Gamma} \int_{z=-1/2}^{z=1/2} \gamma r dr dz \quad , \quad d = \frac{\|\nabla \cdot \mathbf{v}\|}{\|(\mathbf{v} \cdot \mathbf{v})^{1/2}\|} \quad , \end{aligned}$$

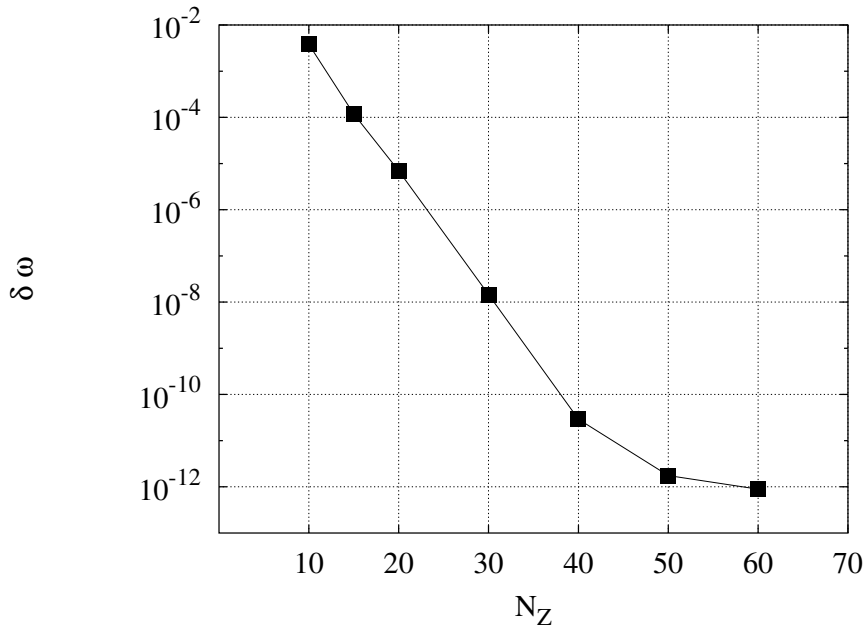


Figure 1: Evolution of the relative error $\delta\omega$ on the angular frequency of a time-dependent flow with grid size $[(2N_z + 1) \times (N_z + 1)]$ nodes in $r \times z$. These values were obtained for a monop periodic flow at $Ra = 2600$, in the $\Gamma = 2$, NS configuration, with a time step δt of 10^{-3} .

where $\|\dots\|$ denotes the infinite norm (i.e: the maximum pointwise absolute value), \mathcal{E} is the kinetic energy in the enclosure, $\bar{\theta}$ and $\bar{\gamma}$ are the global temperature and concentration of the mixture and d is the relative velocity divergence. The evolution of these four quantities with mesh size, for a given steady solution, is given in Table 1. Both $\bar{\gamma}$ and d must asymptotically cancel with increasing N_z , as long as roundoff errors are not taken into account. The reason for this, in the case of $\bar{\gamma}$, comes from solute mass conservation requirement, all boundaries being impervious to matter. Note that such is not the case for $\bar{\theta}$ since nothing imposes that incoming and outgoing heat fluxes should be instantaneously equal. Having no a priori values for $\bar{\theta}$ and \mathcal{E} to compare to, those obtained with the refined grid $N_z = 100$, for which d and $\bar{\gamma}$ are clearly converged, are used as reference. The results given in Table 1 show the expected exponential improvement up to at least $N_z = 60$, followed by saturation due to roundoff effects.

As for the convergence behavior of settled periodic solutions, Fig. 1 displays the relative error

$$\delta\omega = \left| \frac{\omega(N_z) - \omega(N_z = 80)}{\omega(N_z = 80)} \right|$$

on the angular frequency of a test case. Here as well, the exponential convergence with increasing cutoff frequencies is obtained.

All forthcoming results were obtained using grids of (101×51) , (71×71) , (51×101) nodes for the $\Gamma = 2$, 1 and 1/2 configurations. Some results were cross-checked on finer grids of (161×81) , (111×111) and (81×161) nodes, respectively. Resulting shifts in threshold values (even in regions where chaotic flows occur) were of less than 0.05%.

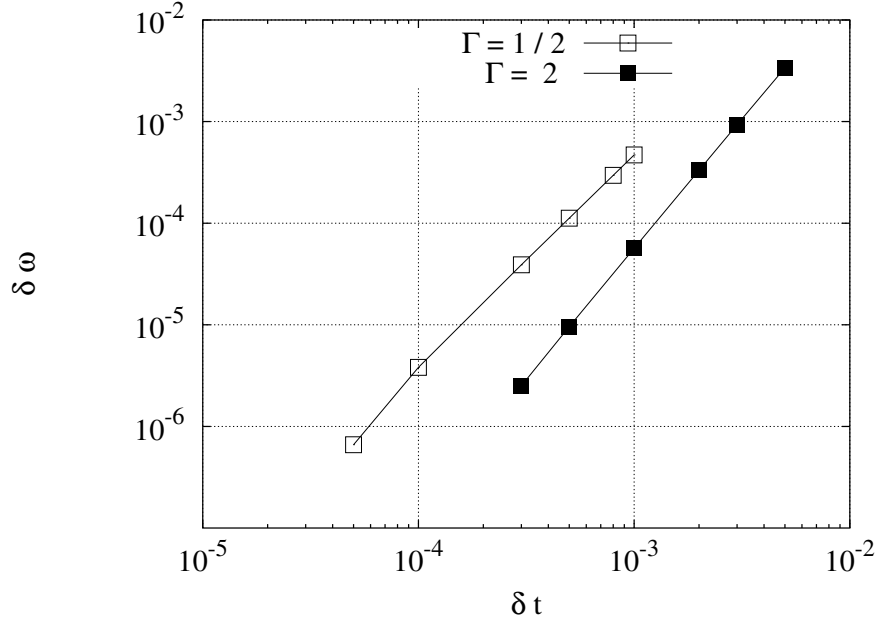


Figure 2: Influence of δt on $\delta \omega$, the relative deviation to our most accurate computations ($\omega = 7.19525440315$ when $\delta t = 3 \cdot 10^{-5}$ for $\Gamma = 1/2$, and $\omega = 7.533299504778$ when $\delta t = 10^{-4}$ for $\Gamma = 2$).

3.2.2 Temporal convergence

Solutions were taken to be stationary when the following criterion was fulfilled,

$$\text{Max} \left(\frac{|\phi_{n+1} - \phi_n|}{|\phi_n|} \right) < 10^{-4} \delta t,$$

where ϕ_n stands for the value of any of the physical fields at dimensionless time $n\delta t$ and Max denotes the maximum evaluated over all fields and nodes.

In the case of time-dependent solutions, a first indication of the effective time-dependency can be extracted from inspection of Poincaré section (see Sec. 4.1). When the solutions seemed to be monophasic, they were deemed so when their instantaneous angular frequency (computed from the return times between successive impacts in the Poincaré section) saturated over its first 8 significant figures.

The time step δt to be used for sufficiently accurate computations of time-dependent solutions was estimated from several test cases such as those given in Fig. 2. The relative deviation $\delta \omega$ to reference ω_{ref} obtained with a “small enough” time step δt is given. It depicts the (expected) second-order temporal convergence of the numerical resolution. The values of δt used to obtain all forthcoming results were chosen to be such that $\delta \omega < 10^{-4}$ for the previously mentioned test cases and are: $\delta t = 3 \cdot 10^{-4}$, 10^{-3} and 10^{-3} for the $\Gamma = 1/2$, 1 and 2 NS configurations and $\delta t = 2 \cdot 10^{-4}$, 10^{-3} and $5 \cdot 10^{-4}$ for the $\Gamma = 1/2$, 1 and 2 FS ones.

4 Results

Results are presented in four steps. The first is dedicated to the analysis of typical transient behaviors and to informations these yield about bifurcation thresholds and types. An

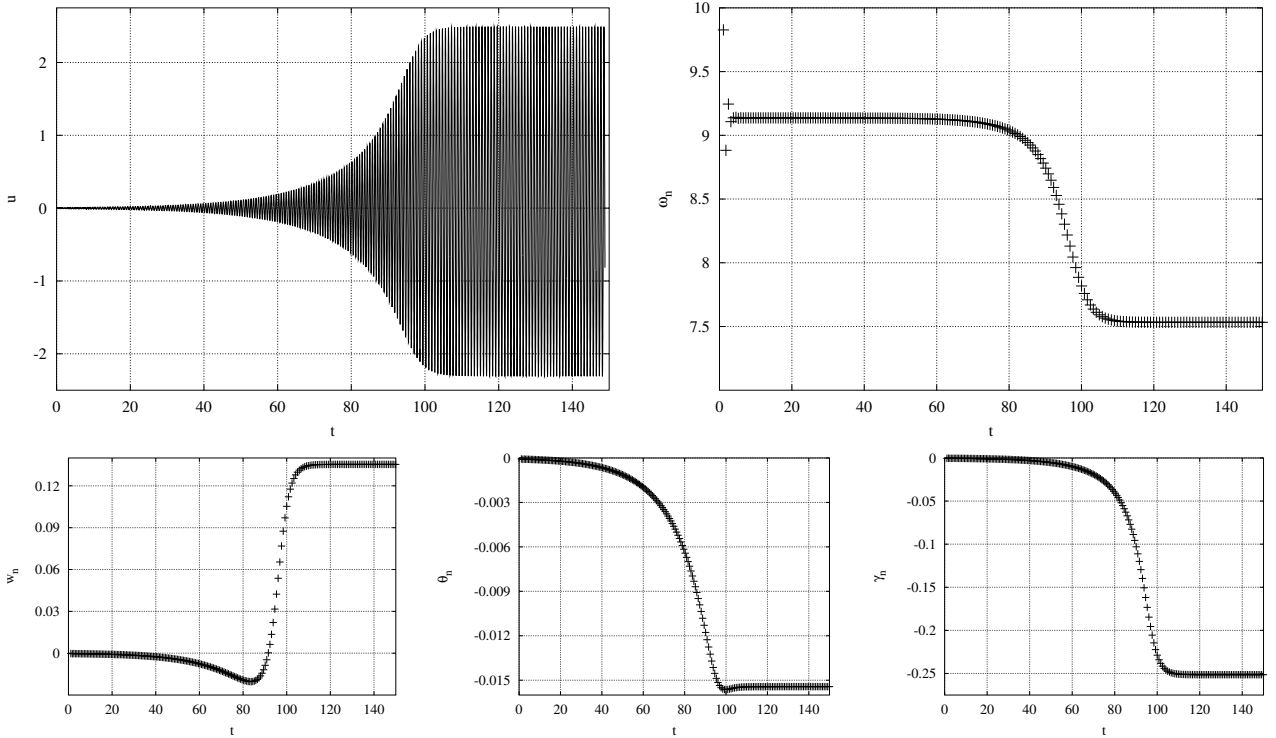


Figure 3: Upper row: Left plot: Evolution of the radial velocity at node P_1 for $Ra = 2600$ in the $\Gamma = 2$, NS configuration. At time $t = 0$ the quiescent state is perturbed by a small random amplitude and the system evolves towards a stable periodic solution. Right plot: Corresponding instantaneous angular frequency ω_n (evaluated from return times τ_n in the Poincaré section, see text). Lower row: vertical velocity w_n , temperature θ_n and mass fraction γ_n in the Poincaré section.

overview of the branches of solutions with their general characteristics is then given, followed by a presentation of the general features of the oscillatory states. Finally, the oscillatory flows' successive bifurcations, up to the transition to steady regimes (also known as Steady Overturning Convection, SOC) are described.

4.1 Transient behaviors

The temporal evolution of the system is followed by monitoring the values of u , w , θ and γ at a pair of z -symmetric nodes P_1 and P_2 , located at $r_{j=2(N_r+1)/3}$ and $z_{j=(N_z+1)/3}$, $z_{j=2(N_z+1)/3}$ respectively.

These time series provide useful information not only about the attractor that is reached (once transients associated with initial conditions die away), but also on the local bifurcations that occur in the system.

In the vicinity of local bifurcations, the temporal evolution about solutions is given by well known and documented (see, e.g., the monographs of Manneville [24] or Ott [25], among others) normal forms. Corresponding transient evolutions are then exponentially growing or decaying with a rate λ linked to both the type of the bifurcation and the distance to the threshold value Ra_{crit} of the control parameter. Thus, in the case of a pitchfork bifurcation, one should have $\lambda \propto (Ra - Ra_{crit})$, as well as for a Hopf bifurcation, where the transient will also display oscillations. For a saddle-node bifurcation, $\lambda^2 \propto (Ra - Ra_{crit})$.

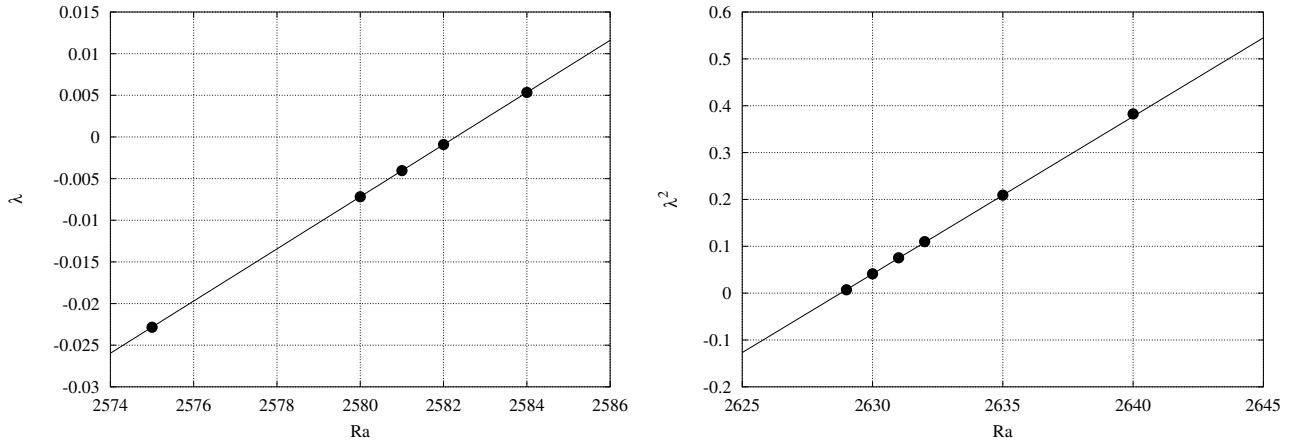


Figure 4: Left: Temporal growth rate λ of infinitesimal perturbations of the conductive state as a function of the Rayleigh number in the vicinity of the Hopf bifurcation of the quiescent state ($\Gamma = 2$, NS configuration). Right: Squared temporal growth rates λ^2 of transient relaxation towards the stationary state close to the saddle-node bifurcation ($\Gamma = 2$, NS configuration). In both cases, the solid line is obtained using the linear law given by the two points that lie closest to vanishing growth rate.

The values of λ (obtained at given values of Ra) can simply be extracted from the time series (monitored at P_1 and P_2) as transients die away and the system settles towards a solution S . This procedure is rather straightforward if S is a steady state. When S is a periodic solution, the transient evolutions from which the aforementioned behaviors are to be extracted come from those obtained in a Poincaré section. The Poincaré section used throughout this study is build from the time series recorded at P_1 . It is defined by the canceling of u , going from negative to positive values, each impact yielding (discrete) time series of w , θ , γ and τ (return time between successive impacts).

An illustration is given in Fig. 3. The time series depicts the evolution of u at P_1 , in a case where the initial condition of the system is a quiescent state (unstable at the Ra value set for this run) perturbed (at $t = 0$) by an $O(10^{-2})$ random amplitude. Since the quiescent solution has turned unstable via a Hopf bifurcation, the perturbation triggers the (linear) Hopf mode. As long as amplitudes remain small ($t < 70$), the transient evolution of the system is an exponentially growing oscillation composed of a single frequency, as shown by the plot of ω_n (angular frequency evaluated from the return times between impacts in the Poincaré section) in Fig. 3. When amplitudes become large, the contribution of nonlinear terms to the dynamics is no longer negligible and the system settles towards a stable periodic solution ($t > 100$). The exponential dying out of the transient, as the latter solution is reached and from which a value of λ can be extracted, is quite obvious in the plots given in Fig. 3.

An example of the feasibility and limitation of following the evolution of λ with Ra in the vicinity of a local bifurcation in order to pinpoint the threshold value from the obtained trends is given in Fig. 4. The expected trend (respectively linear (top) or quadratic (bottom) in the vicinities of Hopf or saddle-node bifurcations) is generally obtained over a small domain in Ra in the vicinity of the bifurcation. Obtaining the $\lambda(Ra)$ trend not only proves that the inferred bifurcation indeed occurs, but yields a more accurate estimation of the threshold

1 NS	A : 3148.5 B : 3079.5 C : 3271.3 D : 3011.5	$\frac{1}{2}$ NS	A : 15167.8 B : 14717 C : 15797.1 D : 14938	2 NS	A : 2582.3 B : 2573.2 C : 2875.7 D : 2628.8
$\frac{1}{2}$ FS	A : 8412.7 B : 8349 C : 8948 D : 8116.8				
1 FS	A : 2434.0 B : 2430.5 C : 2588.8 D : 2326.5				
2 FS	A : 2327.1 B : 2326.5 C : 2551.9 D : 2215.7				

Table 2: Sketches of the three relative positionings of conductive, oscillatory and steady branches of solutions. Top row: Bifurcation diagrams corresponding to the three observed cases. The horizontal line depicts the rest state, ending at a subcritical Hopf bifurcation (A). The middle curve depicts time-dependent states bounded by a saddle-node bifurcation (B) and the transition to SOC (C). The upper curve depicts steady convective states, the lower boundary of which is a saddle-node (D).

value (by definition the value of Ra for which λ cancels) than (necessarily extremely lengthy, due to critical slowing down as $\lambda \rightarrow 0$) direct simulations.

4.2 Branches of solutions

It is well known that, for binary liquids enclosed in extended containers, a sequence of allowed states occurs as Ra is increased, starting from the quiescent state towards steady states after an intermediate oscillatory regime. Each of these states exists over a given domain, thus leading to hysteresis in transitions from one solution to the other. The branches of stable solutions of all the configurations investigated in this work are sketched and categorized in Table 2. Four characteristic points, along with corresponding threshold values are given: A for the end of the rest state branch (subcritical Hopf bifurcation), B (saddle-node) and C (see Sec. 4.4), the extremities of the oscillatory branch and D (saddle-node) the beginning of the SOC domain. The relative positions of points A, B and D was used to categorize results: going from the leftmost to the rightmost column, point D moves from the left of B to the right of A . In all cases, taking a quiescent state to values of Ra above Ra_A triggers the Hopf mode and leads to an oscillatory state. We find that taking an oscillatory solution to Ra values lower than Ra_B always sends the system back to a quiescent state, even if steady convection is also possible for that value of Ra . This reflects the effective extension of the quiescent state's basin of attraction. Configurations given in the leftmost column of Table 2

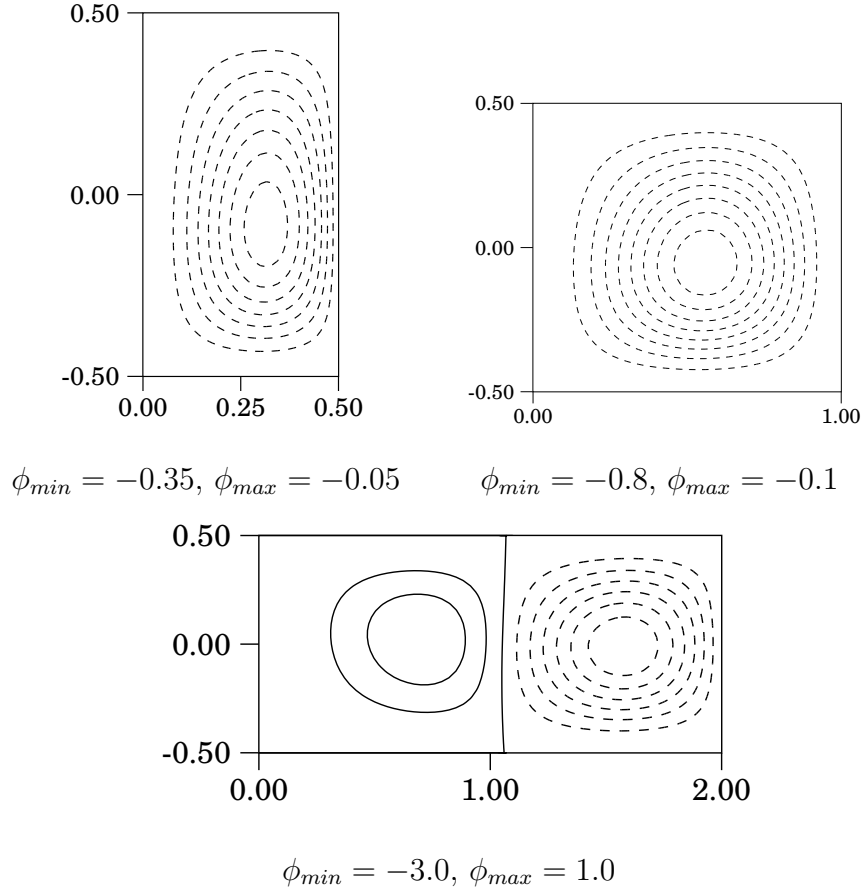


Figure 5: Streamfunction ϕ contours of stationary flows for $\Gamma = 1/2$ (FS configuration, $Ra = 8600$), $\Gamma = 1$ (NS configuration, $Ra = 3300$) and $\Gamma = 2$ (FS configuration, $Ra = 2550$). Solid and dashed lines indicate positive and negative values (clockwise and anti-clockwise motion) of ϕ . Displayed contour levels are evenly distributed and range from ϕ_{min} to ϕ_{max} . Note that the rolls are not even in z and that applying the mirror symmetry \mathcal{M} to the streamfunction is equal to transforming $\phi(r, z)$ into $-\phi(r, -z)$.

are such that the steady state branch extends below the oscillatory one (i.e. $Ra_D < Ra_B$). When $Ra_D > Ra_B$ (middle and rightmost column of Table 2), taking a steady flow to Ra values below Ra_D leads to oscillatory convection. Note that for the $\Gamma = 2$, NS configuration (rightmost column of Table 2), oscillatory convection is the only stable solution for $Ra_A < Ra < Ra_D$. All FS configurations are found to belong to the same category, whereas the NS ones span all three, non-monotonically with Γ .

The evolution of the Hopf thresholds of the rest state (point A in Table 2) with aspect ratio, as well as that of the corresponding Hopf marginal frequencies (given on the plots in Table 3), agree with linear stability results: [10, 11]

1. the values increase slightly from $\Gamma = 2$ to 1 and, obviously, much more dramatically when $\Gamma < 1$;
2. they increase as well going from FS to NS conditions.

Moreover, these trends also hold for all the thresholds of both oscillatory and steady flows.

Before going into a detailed description of the oscillatory branches, we mention here that the steady convective states' characteristics, in the range of Ra values considered, are very similar for a given aspect ratio (1 roll for $\Gamma = 1$ and $1/2$ and a pair of rolls for $\Gamma = 2$) and not sensitive to the choice of boundary conditions. Figure 5 depicts typical flow structures for $\Gamma = 1/2, 1$ and 2 . All SOC solutions do not possess the \mathcal{M} symmetry property and therefore always come in \mathcal{M} -symmetric pairs.

4.3 General features of the oscillatory states

Table 3 depicts the angular frequencies of all the *monoperiodic* oscillatory states, for all Γ and both types of boundary conditions. Going along these curves with increasing Ra values corresponds to following the oscillatory branches of Table 2, from point B up to point C in the NS case or up to the last monoperiodic flow in the FS one.

Point C is not given for the FS configurations in Table 3 as the oscillatory states turn aperiodic before the transition to SOC. These will be described in Sec. 4.4.3. Of the six investigated configurations, only two ($\Gamma = 1$ and $\Gamma = 1/2$, NS) are such that the frequency of the oscillations goes to zero as the transition to SOC is reached.

All time dependent states which stem from B share the temporal symmetry \mathcal{T} . Only in the $\Gamma = 2$, NS configuration is it found to hold over the entire oscillatory domain. In all other configurations, this symmetry breaks down, at point T . This occurs via a supercritical pitchfork bifurcation at the Ra ($= Ra_T$) values given in Table 4. The emerging pair of periodic solutions are \mathcal{M} -symmetric. The proportion of the oscillatory domain over which \mathcal{T} holds is found to increase with Γ in both the FS and NS configurations, which could imply that Γ needs to be smaller than a critical value in order to break the \mathcal{T} symmetry. Another effect, apparently also due to the highly constrained geometry of the enclosure, appears from the inspection of the last column of Table 4: the overlap between stable quiescent and oscillatory branches decreases with respect to the oscillatory domain's extension as Γ increases.

The next section deals with the description of the specific bifurcations that occur in each of the six investigated configurations.

4.4 Successive bifurcations of the oscillatory flows

4.4.1 $\Gamma = 2$, NS configuration

As mentioned in the previous section, in the $\Gamma = 2$, NS configuration, no temporal symmetry breaking occurs. The branch of oscillatory solutions terminates in this case via a subcritical generalized (or secondary) Hopf bifurcation. As Ra is increased towards the bifurcation value, the monoperiodic solutions display transient decaying oscillatory modulations. An example of the evolution of resulting impacts in the Poincaré section given in Fig. 6 where an embedding of the values of w at the $(n+1)^{\text{th}}$ impact versus the n^{th} is shown. The $\{w(n+1), w(n)\}$ sets spiral in towards a final value, according to both growth rate λ and angular frequency of the secondary Hopf mode. The evolution of λ in the vicinity of this bifurcation is given in Fig. 6. At the bifurcation, the secondary Hopf frequency is 0.61, roughly a decade lower than the oscillation's base frequency. Increasing Ra slightly beyond Ra_C , the corresponding monoperiodic solution turns unstable with an initially small modulation arising and growing exponentially. Since the bifurcation is subcritical, the amplitude of the modulation does not saturate (no matter how close to Ra_C Ra may be) and the system is eventually cast towards the nearby stable SOC solutions.

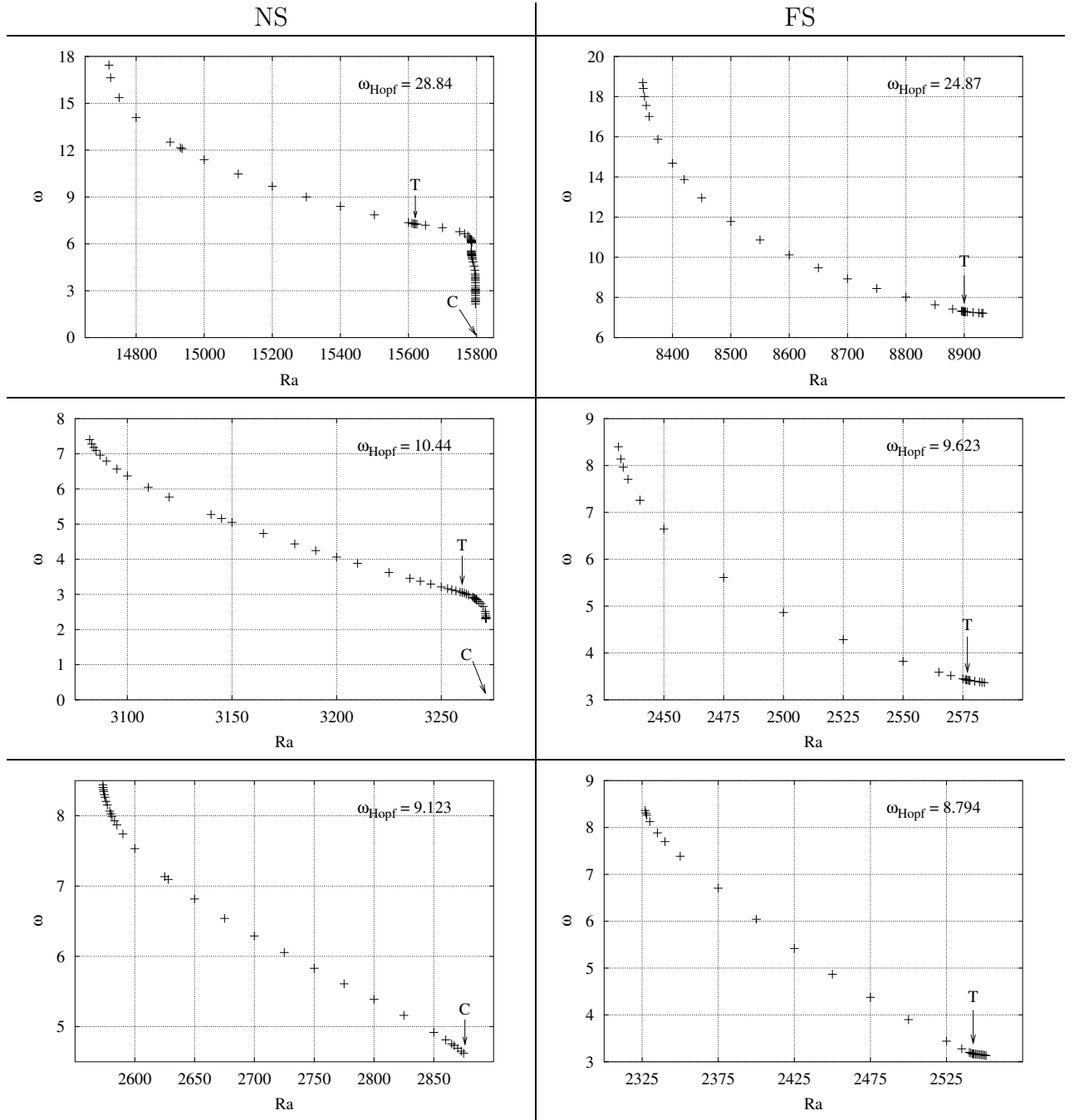


Table 3: Angular frequencies of monoperoic flows. Top row: $\Gamma = 1/2$, middle row: $\Gamma = 1$, lower row: $\Gamma = 2$. Points T and C, when given, indicate the occurrence of temporal symmetry breaking and the transition to SOC (see Table 2).

4.4.2 $\Gamma = 1$ and $1/2$, NS configurations

The $\Gamma = 1$ and $1/2$ configurations have much in common. As previously mentioned, these are the only cases for which the frequency of the oscillations is found to go to zero as the transition to SOC is reached.

As might be guessed from the cluster of points near the end of the oscillatory branches given in Table 3, quite distinctive behaviors occur there. An enlargement of the end of the oscillatory branch ($\Gamma = 1/2$ case) is given in Fig. 7, showing that there are in fact two

Case	Ra_T	$\frac{Ra_T - Ra_B}{Ra_C - Ra_B}$	$\frac{Ra_A - Ra_B}{Ra_C - Ra_B}$
$\frac{1}{2}$ (SF)	8900.5	0.921	0.106
1 (SF)	2577.9	0.931	0.0221
2 (SF)	2542.2	0.957	0.00266
$\frac{1}{2}$ (NS)	15619.7	0.836	0.417
1 (NS)	3260.3	0.943	0.360
2 (NS)	-	-	0.0301

Table 4: Rayleigh number values at which temporal symmetry \mathcal{T} is broken (second column), proportion of the oscillatory domain over which \mathcal{T} holds (third column) and over which both oscillatory and conductive states are stable (fourth column).

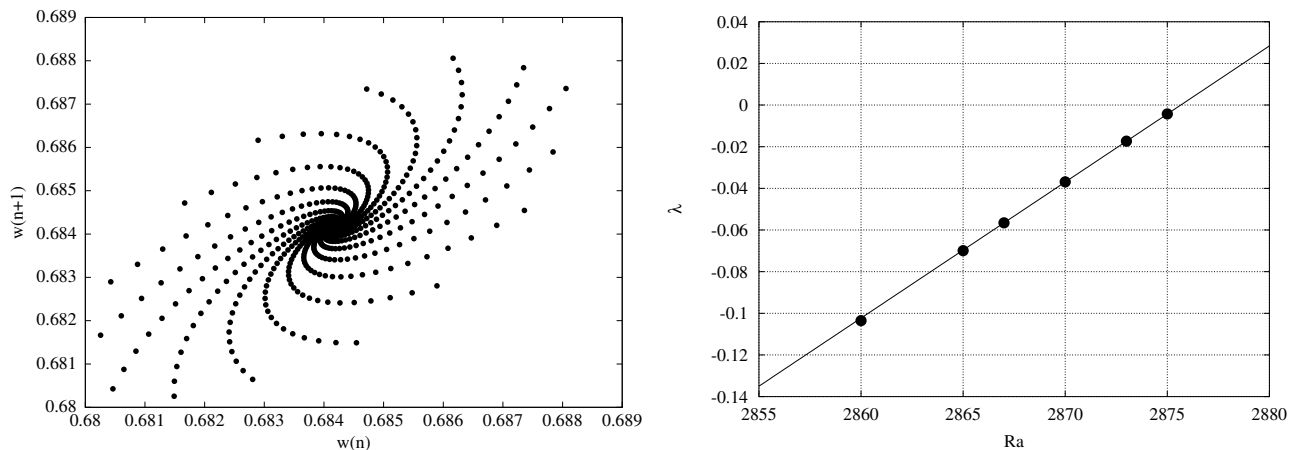


Figure 6: Left: Embedding of the successive values of the vertical velocity w in the Poincaré section, depicting the transient modulation of the periodic state (here, the $Ra = 2875$ flow) by the secondary Hopf mode in the $\Gamma = 2$, NS configuration. $w(n)$ is the value at the n th impact. As time (and therefore n) increases, the $\{w(n+1), w(n)\}$ sets spiral in toward their final value, $w(n+1) = w(n) = 0.6841$. Right: Temporal growth rates λ of the transient modulation of the periodic state as a function of the Rayleigh number, close to the generalized Hopf bifurcation (the solid line is obtained using the linear law given by the two points that lie closest to vanishing growth rate).

branches which overlap over a very narrow range in Ra . Since the upper branch ends in a saddle-node bifurcation and the lower branch begins at one, we conjecture that they are directly connected to each other by an unstable part (obviously inaccessible to our time marching process). Such “bending” of the periodic states branch leading to the coexistence of two stable oscillatory states has also been numerically observed (in mixtures for which $Pr = 10$ and $Le = 0.01$) in extended layers, [9] when $\Psi < -0.4$.

Another important feature depicted in Fig. 7 is the extremely sharp drop in frequency that occurs at the end of the lower branch.

Does the frequency go down to zero as the bifurcation is reached? Such is the case, as indicated by Fig. 8, where the period $\tau = 2\pi/\omega$ versus the distance $Ra - Ra_C$ is plotted, with $Ra_C = 15797.0099$.

The data match a $\tau \propto -\ln(Ra_C - Ra)$ scaling law which meets one of the behaviors obtained in horizontally infinite plane layers (see Knobloch, [26] Knobloch and Moore [27]).

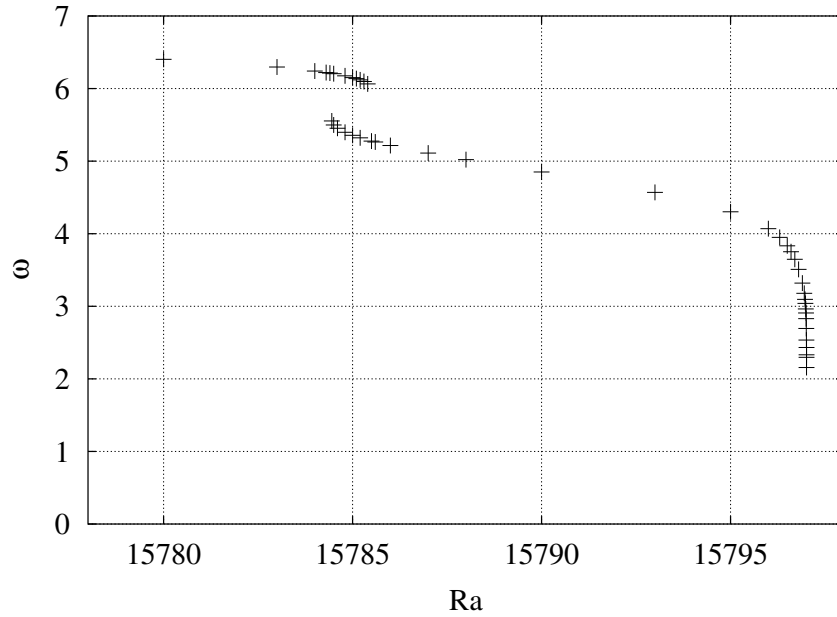


Figure 7: Angular frequencies of periodic solutions at the end of the oscillatory domain, in the $\Gamma = 1/2$, NS configuration.

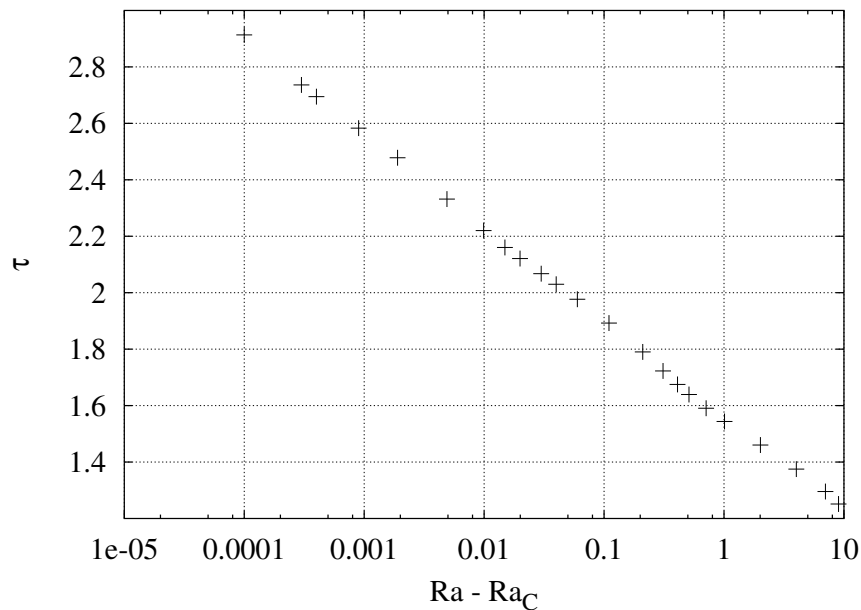


Figure 8: Period τ of the oscillations versus the distance $(Ra - Ra_C)$, where $Ra_C \simeq 15797.0099$) to the homoclinic bifurcation of the periodic orbit ($\Gamma = 1/2$, NS configuration).

In the latter, the transition corresponds to a standing waves branch vanishing in a heteroclinic bifurcation between the limit cycle and a pair of steady state solutions. In the present case, the limit cycle collides with an unstable SOC fixed point in a homoclinic bifurcation which leads to the same scaling. An illustration of this global bifurcation is given in Fig. 9 where phase portraits of the limit cycle prior to the bifurcation and the path followed by the system afterwards are shown.

In unbounded layers, another possible scenario involves traveling waves (TW), the fre-

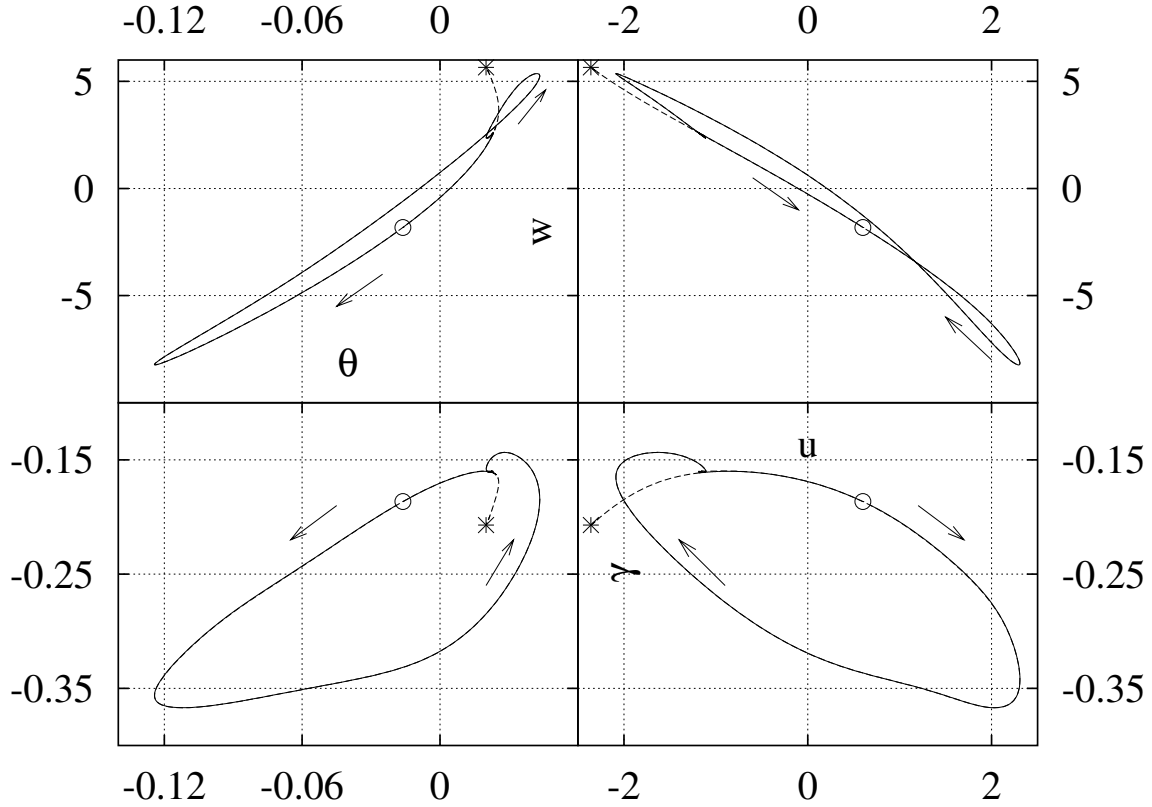


Figure 9: Projections of the phase portrait of the periodic orbit (full line) in the (θ, γ) , (u, γ) , (u, w) and (θ, w) planes, prior ($Ra = 15797.0098$) to the homoclinic bifurcation. The arrows indicate the direction of motion along the orbit. The large dot depicts the initial position of the system when Ra was increased to $Ra = 15797.0099$, slightly above Ra_C . From that point, the system first closely follows the path given by the limit cycle, up to an outset that sends it off (dashed line) towards the stable SOC fixed point (star).

quency of which also vanishes as SOC is reached, but following a $\tau \propto (Ra_C^{TW} - Ra)^{-1/2}$ law. It corresponds to a collision between a group orbit (of SOC solutions, each being neutrally stable with respect to translation) and isolated TW solutions.

This homoclinic bifurcation of the oscillatory branch also occurs in the $\Gamma = 1$ case. The only difference between the $\Gamma = 1$ and $\Gamma = 1/2$, NS configurations is that the branch bending that arises in the latter does not occur in the former.

4.4.3 FS configuration

For all three values of Γ , the sequence of bifurcations that occur with increasing Ra (along with the associated dynamical behaviors) is the following:

1. The first bifurcation occurs at Ra_T , where oscillations lose their temporal symmetry \mathcal{T} via a supercritical pitchfork bifurcation yielding two branches of \mathcal{M} -related periodic solutions.
2. For Ra slightly higher than Ra_T , these oscillatory states undergo a period doubling cascade that leads to chaotic regimes (as shown by the bifurcation diagrams in Fig. 10).
3. In this chaotic region (up to $Ra = Ra_I$) period 7 and period 5 windows are encountered.

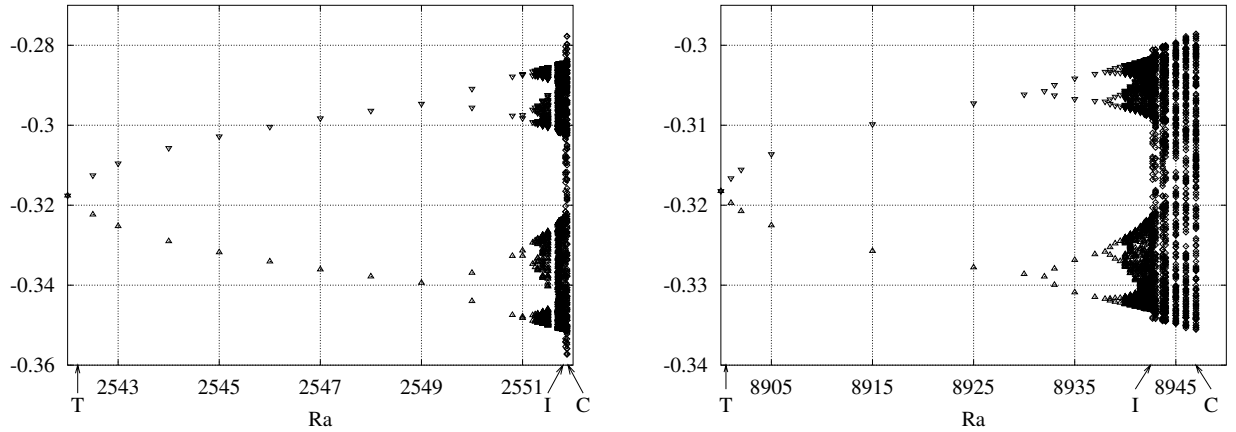


Figure 10: Bifurcation diagrams of the oscillatory solutions, starting from the temporal symmetry breaking up to the boundary-induced crisis (see text). Upward and downward triangles refer to the \mathcal{M} -related states before their merging into a single attractor (diamonds). The upper diagram is obtained for $\Gamma = 2$ and the lower one for $\Gamma = 1/2$. In both diagrams, the values given on the ordinate are those of γ in the Poincaré section.

Period	$\Gamma = 1/2$	$\Gamma = 1$	$\Gamma = 2$
1	8932	2584	2549
2	8933		
2	8935	2584.5	
2	8937	2585	2550
2	8938	2585.5	2550.8
4	8938.5		
4	8939		2551
4	8939.5	2586	2551.2
8		2586.2	2551.25
32			2551.3
C2	8940	2586.5	2551.4

Table 5: Examples of results obtained at given Ra values relative to the period 2 based windows (C2 denotes period 2 based chaos).

4. At Ra_I , crisis-induced intermittency occurs: the separate domains in which the \mathcal{M} -related solutions lived merge and the flow becomes statistically invariant under \mathcal{M} .
5. Chaotic behavior continues until $Ra = Ra_C$ is reached, where there is evidence of a boundary-induced crisis (the attractor becomes “leaky”): after a chaotic transient, trajectories eventually escape, leading the flow to the nearby (SOC) stable fixed point.

Exploring thoroughly the sequences of bifurcation as well as accurately determining the values of thresholds Ra_I , Ra_C and ranges of periodic windows have not been attempted, as such would require considerable amounts of computing time. Hence, the given scenario

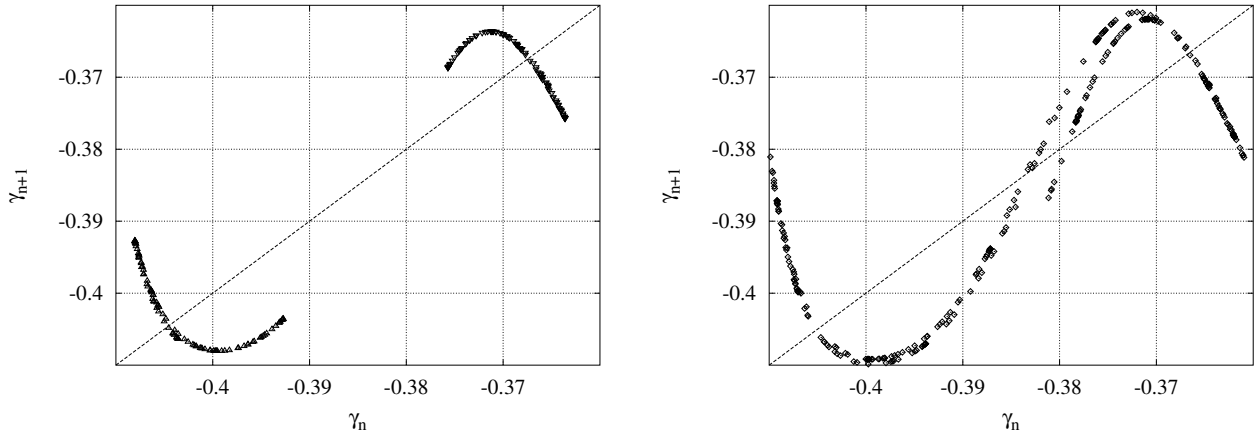


Figure 11: γ_{n+1} vs γ_n Poincaré section return map (from the $\Gamma = 1$, FS configuration), displaying the attracting sets before (upwards and downwards triangles, $Ra = 2586.78$) and after (diamonds, $Ra = 2587.5$) the occurrence of crisis-induced intermittency.

is inferred from obtained results and comparison with typical results detailed in monographs [25, 24] on dynamical systems. For the sake of completeness, we give the following examples:

- In all cases period 2 behavior is indeed found to be followed by period 4, but as the period doubling cascade continues, it does so in a very narrow range in Ra , and intermediate doublings were sometimes missed (see Table 5). A closer look at Poincaré section return maps (such as the ones shown in Fig. 11), along with successive embeddings thereof, shows that, even though the maps are not unimodal, they evolve very much as the standard logistic map does (greater differences do arise beyond the period 2 window). From that, we conjecture that the period doubling cascade is probably complete in all three configurations.
- Similarly, the statement that period 5 and 7 windows occur comes from the combined examination of return maps and results such as landing in one (for instance, period 5 behavior is found at $Ra = 8942$ for $\Gamma = 1/2$ and period 10 occurs at $Ra = 2586.79$ for $\Gamma = 1$) or witnessing related chaotic behavior (at $Ra = 2586.8$ for $\Gamma = 1$ as well as at $Ra = 2551.725$ for $\Gamma = 2$).

It might be worth mentioning here a series of numerical investigations [28, 19, 29] on doubly diffusive convection (in which the Soret effect is neglected and a vertical mass fraction gradient is externally imposed) in 2D Cartesian enclosures of small lateral extension. In these boxes, oscillatory solutions were found to exhibit a rich variety of spatiotemporal behaviors, such as multiple coexisting branches of “bubble” structure (cascades of period doubling bifurcations leading to chaos and followed by reverse sequences which restore simple periodicity). These studies, in which temporal symmetry breaking followed by a cascade of period doubling bifurcations leading to chaotic oscillations is observed, were obtained with free-slip boundary conditions.

5 Conclusions

In this paper, axisymmetric convection of a binary liquid enclosed in a vertical cylinder is investigated. In order to clarify the influence of nearby side boundaries on flow dynamics,

three aspect ratios ($\Gamma = 2, 1$ and $1/2$), as well as either no-slip or free-slip boundary conditions on the cylinder's circumference, are considered.

The oscillatory states are found to undergo various and multiple bifurcations, the occurrences of which strongly depend on the choice of both boundary conditions and aspect ratio. The most significant difference between NS and FS configurations lies in the route to SOC: The oscillatory branches of solutions of NS cases terminate via either a homoclinic (for $\Gamma = 1/2, 1$) or a subcritical generalized Hopf (or Neimark-Sacker) bifurcation (for $\Gamma = 2$), whereas those of the FS cases undergo a period doubling cascade, followed by chaos. It is known [18] that the latter route can only occur for states not possessing the \mathcal{T} symmetry. Moreover, the proportion of the oscillatory domain over which \mathcal{T} does not hold is found to decrease with increasing Γ , much faster in NS than in FS configurations (Table 4). It can thus be conjectured that either all FS cases do bifurcate to SOC in the same way (meaning that the proportion shrinks, but only asymptotically, with Γ), or that there is a critical aspect ratio beyond which the route to SOC will be different. The NS configuration is an obvious illustration of the existence of such a critical aspect ratio Γ_{crit} (about 1.3 from the data in Table 4). Below Γ_{crit} , \mathcal{T} -symmetry breaking occurs: it does not however lead to period doubling but to a (global) homoclinic bifurcation, as the limit cycle collides with an unstable SOC fixed point. Above Γ_{crit} , it is a (local) subcritical Hopf bifurcation of the \mathcal{T} -symmetrical monoperoiodic solutions that leads to SOC.

The dynamical richness of this system is such that some details (e.g. the very small Ra ranges of hysteretic features) are likely to escape experimental investigations, even if extremely carefully designed.

The presence of nearby side boundaries clearly induces significant changes in the dynamical behavior of binary liquid thermal convection.

acknowledgments

We gratefully acknowledge the Centre de Ressources Informatiques de l'Université Paris-Sud for granting us unbounded use of their computer facilities.

References

- [1] M. C. Cross and P. C. Hohenberg, "Pattern formation outside of equilibrium," *Rev. Mod. Phys.* **65**, 851 (1993).
- [2] U. Müller, "Convection in cylindrical containers at supercritical Rayleigh numbers," *PHYSICA D* **97**, 180 (1996).
- [3] R. Touihri, H. Ben Hadid, and D. Henry, "On the onset of convective instabilities in cylindrical cavities heated from below. I. Pure thermal case," *Phys. Fluids* **11**, 2078 (1999).
- [4] B. Hof, P. G. J. Lucas, and T. Mullin, "Flow state multiplicity in convection," *Phys. Fluids* **11**, 2815 (1999).
- [5] S. S. Leong, "Numerical study of Rayleigh-Bénard convection in a cylinder," *Numer. Heat Transfer, Part A* **41**, 673 (2002).
- [6] J. K. Platten and J. C. Legros, *Convection in Liquids* (Springer Verlag, Berlin, 1984).

- [7] P. Kolodner, S. Slimani, N. Aubry, and R. Lima, “Characterization of dispersive chaos and related states of binary-fluid convection,” *PHYSICA D* **85**, 165 (1995).
- [8] W. Barten, M. Lücke, M. Kamps, and R. Schmitz, “Convection in binary fluid mixture. I. Extended traveling-wave and stationary states,” *Phys. Rev. E* **51**, 5636 (1995).
- [9] M. Lücke, W. Barten, P. Büchel, C. Fütterer, C. Hollinger, and CH. Jung, “Pattern formation in binary fluid convection and in systems with throughflow,” in *Evolution of structures in dissipative continuous systems*, edited by F. H. Busse and S. C. Müller (Springer, 1998).
- [10] G. R. Hardin, R. L. Sani, D. Henry, and B. Roux, “Buoyancy-driven instability in a vertical cylinder: binary fluids with Soret effect. Part I: general theory and stationary stability results,” *Int. J. Numer. Methods Fluids* **10**, 79 (1990).
- [11] I. Mercader, M. Net, and E. Knobloch, “Binary fluid convection in a cylinder,” *Phys. Rev. E* **51**, 339 (1995).
- [12] P. Kolodner, “Repeated transients of weakly nonlinear traveling-wave convection,” *Phys. Rev. E* **47**, 1038 (1993).
- [13] O. Batiste, I. Mercader, M. Net, and E. Knobloch, “Onset of oscillatory binary fluid convection in finite containers,” *Phys. Rev. E* **59**, 6730 (1999).
- [14] O. Batiste, M. Net, I. Mercader, and E. Knobloch, “Oscillatory binary fluid convection in large aspect-ratio containers,” *Phys. Rev. Lett.* **86**, 2309 (2001).
- [15] M. Wanschura, H. C. Kuhlmann, and H. J. Rath, “Three-dimensional instability of axisymmetric buoyant convection in cylinders heated from below,” *J. Fluid Mech.* **326**, 399 (1996).
- [16] R. P. Behringer, “Rayleigh-Bénard convection and turbulence in liquid helium,” *Rev. Mod. Phys.* **57**, 657 (1985).
- [17] G. W. T. Lee, P. Lucas, and A. Tyler, “Onset of Rayleigh-Bénard convection in binary liquid mixtures of ^3He in ^4He ,” *J. Fluid Mech.* **135**, 235 (1983).
- [18] J. W. Swift and K. Wiesenfeld, “Suppression of period doubling in symmetric systems,” *Phys. Rev. Lett.* **52**, 705 (1984).
- [19] E. Knobloch, D. R. Moore, J. Toomre, and N. O. Weiss, “Transitions to chaos in two-dimensional double-diffusive convection,” *J. Fluid Mech.* **166**, 409 (1986).
- [20] A. Batoul, H. Kallouf, and G. Labrosse, “Une méthode de résolution directe (pseudo-spectrale) du problème de Stokes 2D/3D instationnaire. Application à la cavité entraînée carrée,” *C. R. Acad. Sci. Paris* **319**, 1455 (1994).
- [21] G. Labrosse, E. Tric, H. Khallouf, and M. Betrouni, “A direct (pseudo-spectral) solver of the 2D/3D Stokes problem: transition to unsteadiness of natural-convection flow in a differentially heated cubical cavity,” *Numer. Heat Transfer, Part B* **31**, 261 (1997).
- [22] E. Leriche and G. Labrosse, “High-order direct Stokes solvers with or without temporal splitting: numerical investigations of their comparative properties,” *SIAM J. Sci. Comput.* **22**, 1386 (2000).

- [23] E. Tric, G. Labrosse, and M. Betrouni, “A first incursion into the 3D structure of natural convection of air in a differentially heated cubical cavity, from accurate numerical solutions,” *Int. J. Heat Mass Transfer* **43**, 4043 (2000).
- [24] P. Manneville, *Dissipative Structures and Weak Turbulence* (Academic, San Diego, 1990).
- [25] E. Ott, *Chaos in Dynamical Systems* (Cambridge University Press, 1993).
- [26] E. Knobloch, “Oscillatory convection in binary mixtures,” *Phys. Rev. A* **34**, 1538 (1986).
- [27] E. Knobloch and D. R. Moore, “Minimal model of binary fluid convection,” *Phys. Rev. A* **42**, 4693 (1990).
- [28] H. E. Huppert and D. R. Moore, “Nonlinear double-diffusive convection,” *J. Fluid Mech.* **78**, 821 (1976).
- [29] D. R. Moore, N. O. Weiss, and J. M. Wilkins, “Asymmetric oscillations in thermosolutal convection,” *J. Fluid Mech.* **233**, 561 (1991).